

The fixed probe storage ring magnetometer for the Muon g-2 experiment at Fermi National Accelerator Laboratory

E. Swanson^a, M. Fertl^{a,b}, A. Garcia^a, C. Helling^a, R. Ortez^a, R. Osofsky^a, D. A. Peterson^a,
R. Reimann^b, M. W. Smith^a, T. D. Van Wechel^a

^aUniversity of Washington, Box 351560, Seattle, WA 98195, USA

^bJohannes Gutenberg University Mainz, 55128 Mainz, Germany

Abstract

The goal of the FNAL E989 experiment is to measure the muon magnetic anomaly to unprecedented accuracy and precision at the Fermi National Accelerator Laboratory. To meet this goal, the time and space averaged magnetic environment in the muon storage volume must be known to better than 70 ppb. A new pulsed proton nuclear magnetic resonance (NMR) magnetometer was designed and built at the University of Washington, Seattle to track the temporal stability of the 1.45 T magnetic field in the muon storage ring at this precision. It consists of an array of 378 petroleum jelly based NMR probes that are embedded in the walls of muon storage ring vacuum chambers and custom electronics built with readily available modular radio frequency (RF) components. We give NMR probe construction details and describe the functions of the custom electronic subsystems. The excellent performance metrics of the magnetometer are discussed where after 8 years of operation the median single shot resolution of the array of probes remains at 11 ppb.

Keywords: pulsed nuclear magnetic resonance, magnetic field, muon, anomalous magnetic moment

1. Introduction

The measurement of the muon magnetic anomaly, a_μ tests the predictions of the Standard Model of Particle Physics (SM) and relies on a high accuracy determination of the magnetic field in the muon storage ring. The BNL E821 experiment at Brookhaven National Laboratory, Upton, New York, USA, measured a_μ between 1997 and 2001 [1] with a accuracy of 550 ppb. E821 employed a super-ferric storage ring magnet, shown in cross-section in figure 1. The super conducting magnet operates in non-persistence mode at a field of 1.45 T in the toroidal muon storage volume (major radius $R = 7.112$ m and minor radius $r = 4.5$ cm). The pulsed proton NMR systems developed for and employed in the BNL E821 experiment consist of an in-vacuum *magnetic field trolley* and a system of distributed NMR probes at fixed locations above and below the muon storage region (shown in figure 1) for continuously monitoring the field. The trolley is

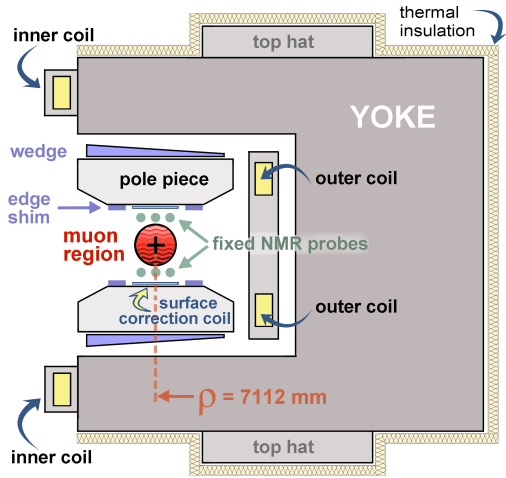
deployed throughout the muon storage volume and maps the magnetic field when muons are not being stored in the ring. Magnetometer field measurements are given in terms of proton spin precession frequencies. These come from directly averaging zero crossing time intervals of free induction decay (FID) waveforms in hardware. E821 systems are further described in reference [2]. A separate precision NMR magnetometer, based on well known properties of protons in water [3], provided the absolute field calibration for the measurement.

In 2013, the super-ferric muon storage ring was transported to Fermi National Accelerator Laboratory, Batavia, Illinois, USA to serve a second life as the heart of the new FNAL E989 experiment. The new experiment aims to achieve a 4-fold reduction in uncertainty (140 ppb) on a_μ . To achieve this goal, the measurement precision and accuracy of the 1.45 T magnetic field will need a twofold improvement over the E821 measurement [4].

The FNAL E989 *fixed-probe magnetometer* is conceptually similar to the one deployed in E821, but with redesigned NMR probes and electronics. In contrast to E821, the magnetometer provides

*Corresponding author: Tel.: +1-206-543-4080.

Email address: eriks@uw.edu (E. Swanson)



g-2 Magnet in Cross Section

Figure 1: Cross section view of the super-ferric muon g-2 storage ring magnet. The open part of the magnet's yoke faces the center of the ring. Between the upper and lower pole pieces is the muon storage region with magnetometer NMR probes located above and below. Pole pieces are individually shimmed to produce a homogenous azimuthal magnetic field.

actual digitized FID waveforms for extracting precession frequencies by subsequent analysis to better understand the magnetic environments of the probes [5].

Here we present design details of the new fixed probe magnetometer, the redesigned NMR probes and associated pulsed radio-frequency electronics. The in-vacuum trolley was refurbished and significantly upgrade, as described in reference [6]. The NMR probes (described in section 3) were also used for the trolley system. Lastly, reference [7] describes the design and development of the new water-based probe used for absolute magnetic field calibration in E989, which has been cross-calibrated by a hyperpolarized ^3He probe [8].

2. Nuclear magnetic resonance

The accurate determination of the storage ring magnetic field relies on pulsed proton NMR. The technique used here is best described in storage ring magnet coordinates. Observing the ring in cross section in figure 1, \vec{B}_0 defines the vertical y -direction of a locally Cartesian coordinate system. The positive x direction is pointing to the center of the ring (left in the figure) and z points

out of the page in the direction of travel of the muon beam. For protons exposed to a magnetic flux density B_0 , the Larmor frequency is $\nu_L = B_0 \frac{\gamma_p'}{2\pi}$, where γ_p' is the gyro-magnetic ratio of the protons in the sample material. For a single free proton $\gamma_p/2\pi = 42.577\,478\,518(18)$ MHz/T [9].

Here we employ the classical vector description of NMR [10] in which the macroscopic equilibrium magnetization \vec{M} of the proton sample is given by

$$\vec{M} = P_0 N \mu_p \hat{B}_0, \quad (1)$$

where N is the number density of magnetic moments, P_0 is the polarization of the material, μ_p the magnetic moment of the individual proton in the sample material and \hat{B}_0 the unit vector in the direction of the magnetic field. The orientation of \vec{M} can be manipulated with oscillating magnetic fields of frequency ω . The effect of oscillating magnetic fields can be conveniently described in a coordinate system co-rotating with frequency ω around \hat{B} . For a magnetic RF field \vec{B}_1 oriented perpendicular to \vec{B}_0 the magnetic field \vec{B}_{cr} in the co-rotating coordinate system is given by

$$\vec{B}_{\text{cr}} = \vec{B}_1 + \vec{B}_0 \left(1 - \frac{\omega}{\omega_L}\right). \quad (2)$$

On resonance $\omega = \omega_L$ the contribution of the static external magnetic field \vec{B}_0 vanishes. Then the direction of the effective magnetic field \vec{B}_{cr} is given by \hat{B}_1 . In the co-rotating frame, the magnetization vector will in general be rotating around the direction of \vec{B}_{cr} . If the RF pulse is applied on resonance and for the time $t_{\frac{\pi}{2}} = \frac{\pi}{2\gamma_p B_1}$ the magnetic moments will be tilted by 90° into the x - y plane of the co-rotating frame. A pulse of this duration is referred to as the $\pi/2$ pulse. In the laboratory frame the magnetization will thus precess with the Larmor frequency $\omega_L/2\pi$. The general time evolution of the magnetization vector can be described by the Bloch equations [11]

$$\frac{M_{x,z}}{dt} = \gamma_p \left(\vec{M} \times \vec{B} \right)_{x,z} - \frac{M_{x,z}}{T_2} \quad (3)$$

and

$$\frac{M_y}{dt} = \gamma_p \left(\vec{M} \times \vec{B}_0 \right)_y - \frac{M_y - M_0}{T_1} \quad (4)$$

with the longitudinal relaxation time T_1 and the transverse relaxation time T_2 . T_1 governs the maximum measurement repetition rate. The proton

sample is surrounded by a coil which forms the inductor of a series resonant LC circuit. The coil acts as the excitation coil when delivering the RF pulse and as a pick-up coil in which the excited precession of \vec{M} induces an electromotive force according to Faraday's law. The resulting waveform is the free induction decay or FID.

3. NMR probes for the fixed-NMR-probe array and trolley

Detailed visual inspections and electrical tests of the NMR probes employed by the BNL E821 experiment revealed that most of these probes had failed from mechanical and/or electrical reasons by the time they had been removed from the E821 setup or potentially even earlier. E821 probes used water doped with CuS for their proton rich material which evaporated over time affecting FID signals. To meet performance goals, new substantially upgraded NMR probes for both the fixed-NMR-probe array and the *magnetic field trolley* were developed and built to address the identified failure modes. The NMR probes described here use petroleum jelly for their proton rich material. Petroleum jelly has a longitudinal relaxation time T_1 of 30.5 ms which is comparable to that of doped water and does not evaporate. NMR studies done at the University of Washington at high fields resolved two separate protons in petroleum jelly, but that difference is small enough that they are not resolved at ring fields and the measured temperature dependence was a few ppb. The nominal storage ring field of 1.45 T was determined by muon beam dynamics, and probe tuning is limited to a narrow field measurement range about this value by design.

3.1. Mechanical and electrical design considerations

An important design consideration of NMR probes used in both the fixed-NMR-probe array and the *magnetic field trolley* is their long-term stability and reliability over the multi-year physics data taking period of FNAL E989. Individual probes in the fixed-NMR-probe array are only accessible by removing a complete vacuum chamber section from the experiment. For *magnetic field trolley* probes, the muon storage volume first needs to be brought to atmospheric pressure and the *magnetic field trolley* removed and unsealed to access individual probes. Any changes in probe positions from

this process invalidates their calibrations. Both procedures are prohibitively time-consuming. The implemented design upgrades include

- a more stable mechanical layout that allows a wide-range frequency tuning of the resonance circuit without inducing mechanical stress on the probe assembly.
- electrical crimp connections on the cable and on the parallel inductor with reduces contact resistance and increased mechanical and electrical long-term stability.
- ultrasonic soldering of aluminum to copper connections.
- the exclusive use of non-corrosive petroleum jelly as the proton sample which avoids proton sample leakage (resulting in signal loss) and corrosion of probe construction materials.

The exterior dimensions of the probes were limited by the milled-in slots of the E821 vacuum chambers, which were re-used in E989. The choice of construction material was strictly limited to non-ferromagnetic materials.

3.2. Mechanical design details

Here we present details of the mechanical design. A detailed description of the assembly process of an individual NMR probe is given in appendix 7.1. A cut away view of the mechanical design of the NMR probe body is shown in figure 2. Each NMR probe has a cylindrical shape of 8.00 mm outer diameter (OD) and a total length of 100.0 mm. The inner mechanical backbone of the NMR probe is provided by the *sample holder*. Made from polytetrafluoroethylene (PTFE), the *sample holder* accommodates a coaxial cylindrical cavity of 2.5 mm diameter and 31.7 mm length filled with petroleum jelly as the active proton sample. A 32-turn coil (Essex, GP/MR-200, AWG 30 magnet wire, copper) is wound around the center of the bubble-free petroleum jelly sample into cut grooves structured with a M4.5x0.5 external thread of 15.00 mm length (thread outer diameter 4.60 mm). This coil is the inductor of the series LC circuit. The connecting ends of the inductor run embedded under the surface of the *sample holder* in a straight groove (depth $0.99^{+0.03}_{-0.00}$ mm, width 0.28 mm) to preserve the cylindrical surface and to avoid electrical shorts to the aluminum sleeve. At the top of

the *sample holder*, a double-threaded aluminum (Al6061) cylinder, screwed into an M3 thread, seals the petroleum jelly sample cavity. One end of the coil is soldered into a wire eye formed from a bare copper wire. The bare copper wire is soldered into a through hole in the aluminum conductor using an ultrasonic soldering technique [12] for low resistance electrical contact and longevity. The lower end of the *sample holder* a coaxial recess (OD 4.00 mm, length 9.00 mm) accommodates a second parallel inductor coil used to impedance-match the driven end of the LC circuit to the $50\ \Omega$ impedance of the double-shielded non-magnetic RF cable (Huber & Suhner GS 02232 D). The *sample holder* screws into a M4x0.5 internal thread (depth 6.00 mm) in the *base piece* around the dielectric and inner conductor of the RF cable which enters the NMR probe through coaxial holes in the *base piece* (diameter 1.6 mm) and the *sample holder* (diameter 1.9 mm). The *base piece* provides the electrical connections for the RF cable outer conductor and the parallel inductor coil. For good electrical and mechanical stability, both connections are crimped. The bare end of parallel inductor coil wire (Essex, GP/MR-200, AWG 28, bare diameter 0.32 mm) is placed in a partially cut open off-axis hole (center radial position 2.45 mm, diameter 0.4 mm) in a cylindrical step (diameter 5.00 mm) in the *base piece*. The wire is secured in the hole in the radial direction while the wire's surface rises 0.11 mm above the cylindrical surface of the *base piece* and is crimped in place with an *inner crimp ring*. This *inner crimp ring* (inner diameter (ID) 5.00 mm, OD 6.00 mm, length 3.00 mm, Al1100) is slightly undersized compared to the maximum dimension across the assembly dimension at the wire location of 5.15 mm. During the installation, the *inner crimp ring* is pressed over the wire/base piece connection which pinches the wire permanently in place. The applied force also breaks up the aluminum oxide layer, which reduces the local contact resistance. The outer conductor of the double-shielded cable is mechanically and electrically connected by crimping the *outer crimp ring* (ID 3.60 mm, OD 4.40 mm, length 7.0 mm, Al1100) onto the RF cable feed-through section (OD 2.70 mm) of the *base piece*. The assembly of *sample holder*, *base piece* and RF cable is inserted into a precision sleeve (OD 8.00(10) mm, ID $7.000^{+0.005}_{-0.000}$ mm, length 97.00 mm) made from 99.5% aluminum bought from alu-verkauf.de. The tight fit between the aluminum sleeve and the *base piece* (OD of mating surface $7.000^{+0.000}_{-0.010}$ mm)

provides mechanical stability and good electrical contact. The latter is significant because the aluminum sleeve influences the inductance of the series inductor coil (due to induced mirror surface currents) and is also the outer conductor of the tuneable cylindrical capacitor of the LC circuit. Its capacitance is adjusted by changing its dielectric filling factor. The position of a thin PTFE cylinder with internal thread (M5x0.5) can be adjusted along the length of the *inner conductor* with an external thread (M5x0.5). For good position control, the *inner conductor* has a rectangular groove in its end face which allows locking its angular position in place while rotating the PTFE dielectric with a custom screwdriver. The hollow screwdriver clears the *inner conductor* and engages with two teeth in two grooves in the front face of the PTFE dielectric. The development of the special screwdriver was key to performing the PTFE position adjustment after the NMR probe was fully assembled, without risk of breaking the solder joint between the *inner crimp ring* and the parallel inductor coil wire. The NMR probe is physically and electrically closed by an aluminum cap. Due to the proximity of the cap to the *inner conductor* there is a small extra contribution to the capacitance of the capacitor. A threaded hole (M3x0.5) in the outer face allows for easy removal of the cap for the frequency tuning procedure. To that end, a plastic screw is inserted in the thread. The plastic screw is used to co-axially pull out the end cap to avoid deformation of the soft precision aluminum sleeve.

4. The pulsed NMR electronics system

The NMR electronic systems generate and deliver RF excitation pulses to the 378 NMR probes and receive and process FID signals before they are digitized for further analysis. Figure 3 shows a block diagram of the individual components of the NMR magnetometer. The design employs two custom electronic modules: *pulser-mixers* which are 1-U-wide NIM modules located in the low-magnetic field region at the ring center and *multiplexers*, stand alone units on top of the storage ring magnet that connect to individual probes. These are shown within the shaded regions of figure 3. Modular RF components, readily available from MiniCircuits (MC), are used as building blocks for magnetometer circuits. The pulsers (the pulse shape forming box in the figure) form the timed burst of 61.74 MHz RF ($\pi/2$ pulse) from a clock synthesizer and send

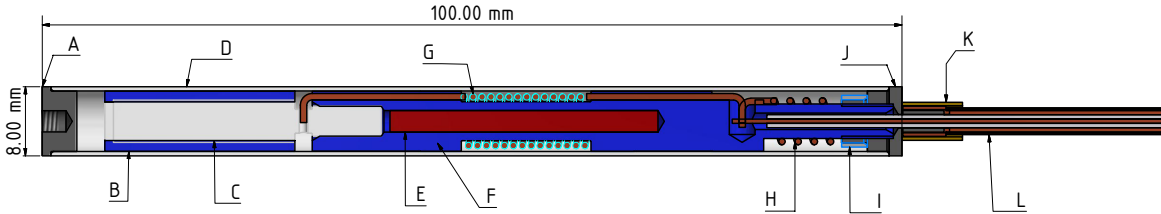


Figure 2: Cut-away view of the mechanical design of the NMR probe. The mechanical backbone of the probe is the *sample holder* (F), made from PTFE, which provides mechanical stability to the serial (G) and parallel (H) inductor coil. The *sample holder* accommodates the petroleum jelly sample (E) which is sealed off by the *inner conductor* (C) of the tune-able cylinder capacitor. Its capacitance is determined by the dielectric fill factor between the inner conductor and the aluminum sleeve (D) acting as the outer conductor. The position of the PTFE dielectric (B) is used to change the fill factor of the capacitor. The parallel inductor coil is mechanically and electrically connected to the *base piece* (J) with the *inner crimp ring* (I). The *outer crimp ring* (K) is used to crimp the outer conductor of the double shielded RF cable (L) to the *base piece*. The NMR probe is mechanically closed with an end cap (A).

them to multiplexers where they are further amplified to 10 W to excite the 61.79 MHz Larmor resonance in the selected NMR probes. The pulse width ($\tau \approx 7\mu\text{s}$) is sufficiently short that its Fourier Lorentzian width ($1/\tau$) overlaps the Larmor resonance with enough power to excite the resonance. Using this same clock, the mixer down-converts the amplified and returning NMR waveforms to about 50 kHz for digitization by the waveform digitizers (WFDs). 61.74 MHz is then added back in the analysis. Twenty pulser-mixer-multiplexer combinations (24 channels per multiplexer) are used to read out all 378 NMR probes of the fixed-NMR-probe array. In the following sections we present details of the individual components.

4.1. The frequency standard and frequency synthesizer

For all measurement systems in E989, RF signals are derived from a common 10-MHz GPS disciplined SRS FS725/1C frequency standard that provides a continuous-wave sinusoidal signal. For the magnetometer system described here it provides the reference standard for the frequency synthesizer and the sample clock for the waveform digitizers. The 61.74 MHz signal used to form the RF pulse to excite the FID and for mixing the FID signal down to the digitization frequency is generated by an SRS SG 382 frequency synthesizer. Video distribution amplifiers distribute this signal to the 20 pulser-mixer modules.

4.2. Pulser-Mixer NIM module

The block diagram in figure 4 shows the RF signal processing architecture which uses active and passive modular RF components. Individual part numbers given in the text are from the Mini-Circuits catalog [13]. The lower branch corresponds to the pulser and the upper branch to the mixer. Common to both, the 10 dBm 61.74 MHz reference signal is amplified with the combination of a GVA-81+ 10.5 dB amplifier and LAT-6 attenuator for a net power increase of 4.5 dB. When split two ways with the ADP-2-1W this provides 11 dBm of power each for pulser and mixer branches of the diagram.

4.2.1. Pulser

The pulser is used to form a combined control and excitation RF pulse of low power and adjustable length. A one-shot multivibrator (74HC221) (figure 4) triggered by a TTL signal from the VME FPGA subsystem of the DAQ generates an adjustable width TTL pulse in the range $6\mu\text{s}$ to $16\mu\text{s}$ which controls a reflective single-pole-double-throw (SPDT) solid state switch (VSW2-33-10W+) connected to the 61.74 MHz signal from the splitter. The total pulse length is determined by the time required to set up the RF switch-yard for high-power and the length of the RF excitation pulse $t_{\pi/2}$. This feeds the variable attenuator block consisting of an LAT-3 fixed attenuator and MVA-2000+ voltage variable attenuator with its control voltage range centered on a nominal value of -10.3 dB. The

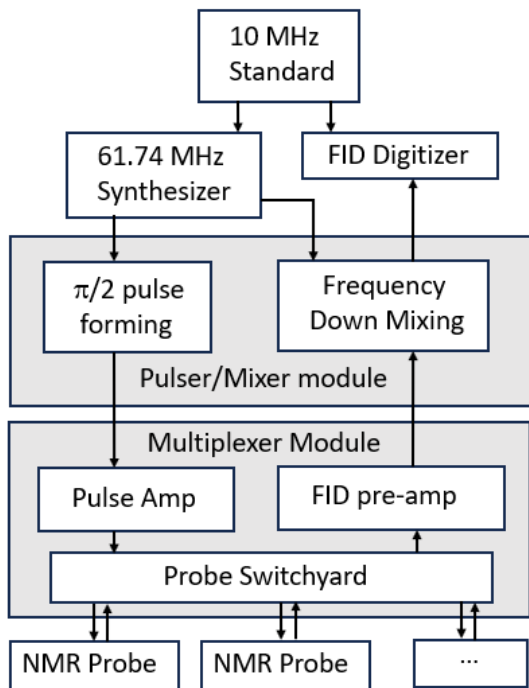


Figure 3: Block diagram showing the NMR magnetometer. At the top are the GPS disciplined reference, the 61.74 MHz frequency synthesizer and waveform digitizer. The two shaded blocks are pulser/mixer and multiplexer modules. The pulser/mixer generates the $\pi/2$ excitation pulse and down converts the returning FID for digitization. The DAQ provides a trigger to simultaneously initiate the $\pi/2$ pulse and start the waveform digitizer. In the multiplexer module the selected probe is first connected to the pulse amplifier to excite the resonance and then to the preamplifier which sends the FID back to the mixer.

subsequent gain block boosts the output power to 10 dBm for transmission to the multiplexer.

4.2.2. Mixer

The pre-amplified FID signal from the multiplexer (figure 4) has a maximum power of +1 dBm at the input to the mixer. This is increased to 15.3 dBm by the combination of a LAT-1 attenuator and a GVA-82 15.3 dB amplifier. The switch inhibits the returning FID during the RF pulse to avoid saturation of downstream signal-processing components. Signal bandwidth is limited with a BPF-B63+ (63 ± 2) MHz band pass filter. The FID signal at the RF input of the ADE-1+ mixer (circle with X) has a maximum power of 0 dBm which is 15 dBm below the third-order intercept point (IP3). Reference signal power is increased to 17.5 dBm with a GVA-81 and LAT-4 combination and then attenuated by a LAT-10 (10 dB) to drive the LO input of the device at 7 dBm. The LO input of the mixer has a 2.5 voltage standing wave ratio (VSWR) and the 10 dB attenuator provides isolation from the reflected signal. An active low-pass filter section removes the sum frequency component in the IF output signal and amplifies the approximately 50 kHz difference frequency for the WFDs. Four cascaded filter stages using Analog Devices ADA4898-1 operational amplifiers make up the low-pass filter section. The first stage is a first-order low-pass filter with a cut-off frequency of 150 kHz and a non-inverting gain of 10. The next two stages are second-order low-pass filters (Sallen-Key topology) with cutoff frequencies at 155 kHz and 177 kHz respectively and Q-factors of 0.5. These each have non-inverting gain factors of 1.2. The final stage brings the nominal gain of the filter at 50 kHz to 25, which is further adjusted to match the input voltage range of the WFDs.

4.3. Multiplexer Module

The multiplexer module, (block diagram shown in figure 5), includes a switchyard for selecting one of 24 NMR probes and connecting it to the pulser or the mixer signal paths (T/R switch in the diagram), a low noise preamplifier to boost the FID signal for the mixer and a 10 W pulse amplifier for exciting the probe. RF signal switching throughout the multiplexer uses VSW2-33-10W SPDT (MC) reflective mode field-effect transistor (FET) switches rated for 10 W continuous power, with 0.5 dB insertion loss and 40 dB isolation when switched off.

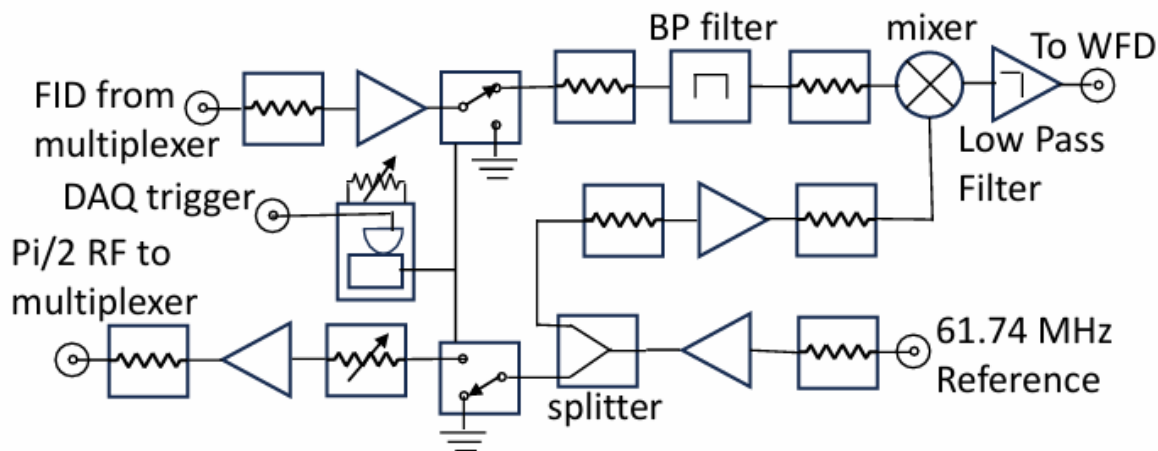


Figure 4: Block diagram showing pulser and mixer circuits using modular RF components. Blocks consisting of fixed gain amplifiers (triangles) and attenuators (resistor symbols) provide signal gain and isolation. In the lower right the frequency reference is split between pulser (bottom) and mixer (top) signal paths. Pulse width is determined by a one-shot multivibrator that controls SPDT RF switches in the reference and returning signal paths. A switch (not shown) selects between the one-shot and the DAQ trigger pulse width. A voltage variable attenuator controls the output amplitude of the pulse. FID signals are band pass filtered, mixed down to about 50 kHz and further amplified and filtered with a 4 stage low pass filter for the waveform digitizers (WFD).

4.3.1. Probe Switchyard

The reflective mode probe switches connect a common signal bus between individual NMR probes when closed or present a high impedance when open. Figure 6 is a section of the switchyard schematic diagram showing two banks of probe switches: the bank select switch, and the transmit-receive switch (see T/R figure 5) that connects selected probes to either the pulse amplifier or preamplifier. Grouping switches in two separate banks reduces signal loss from the combined input capacitance of all the switches. The T/R switch is controlled in a coordinated way with the pulse amplifier to ensure switch transitions occur at low power. Section 4.3.2 describes this in detail. 5-bit ASCII addresses from the Data Acquisition (DAQ) VME interface encode the probe selection. Each of the five signals are filtered with an RC time constant of 12 μ s. The signal line is further attached to a 74HCT541 octal buffer. The two low order bits are input to six 74HC139 2 to 4 line decoders that select one of four probes in each of six groups of switches. The remaining higher order bits connect to one 74HC138 3 to 8 line decoder, which selects one of the 6 groups. An OR of the first 3 74HC138 decoder lines (groups 1, 2, and 3) controls the switch selecting the probe bank. Front panel LEDs on the

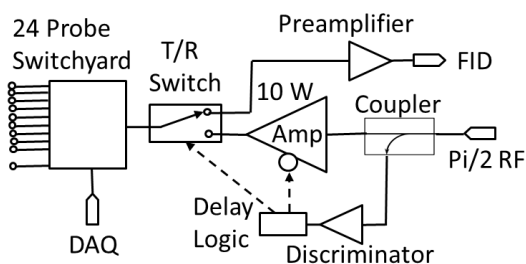


Figure 5: Block diagram showing multiplexer components. The multiplexer serves as a switchyard for accessing individual NMR probes, increases pulse power to 10 W and provides low noise pre-amplification of the returning FID signals. The transmit-receive switch (T/R) determines the direction of power flow within the probe and is controlled by a network that prevents applying power until after the switch changes state.

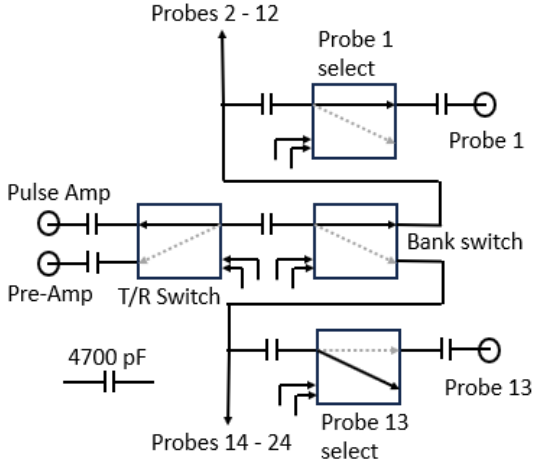


Figure 6: A partial schematic diagram of the probe switchyard and Transmit/Receive (T/R) switch in the multiplexer module. Individual probes are grouped in two banks of twelve probes with each probe selected through the setting of the bank switch and an individual probe select switch. The T/R switch determines the direction of power flow in the probes, either from the 10 Watt amplifier or to the low noise preamplifier. Blocking capacitors are 4700 pF and switches are controlled by TTL signals and their complements. Circuit is shown selecting probe 1 for excitation by a $\pi/2$ pulse.

multiplexer show the selected probe channel.

4.3.2. Pulse Amplifier

The pulse amplifier (PA) increases RF pulse power to 10 W, achieving a 90° rotation of the proton spins away from vertical in about $7\mu\text{s}$. This is short compared to the decoherence time T_2^* , which is largely determined by the homogeneity of the magnetic field environment. Actual pulse widths come from maximizing FID waveforms. Amplification proceeds in two stages, a driver and an output power amplifier. The output stage uses an NPA1006 (MACOM <https://www.macom.com/products/product-detail/NPA1006>) GaN D-mode amplifier operating as a broadband linear amplifier with output power controlled through application of a gate-source bias voltage. A long-tailed pair, with one input controlled by a TTL signal, switches between the -5V required for pinch off and an adjustable value between -5V and -0.5V for 10 W-power operation. The output passes through two cascaded π section low pass filters with 115 MHz cutoffs, which is below the second harmonic of the 61.74 MHz excitation frequency. The driver stage uses a TQP7M9105 (QORVO

www.qorvo.com/products/p/TQP7M9105) with a power output of 1 W and gain of 17.9 dB. The NPA1006 and driver stage have a combined gain of 28.9 dB. To achieve 10 W-operation, the 10 dBm RF signal from the pulser (section 4.2.1) requires an additional 10 dB of amplification to compensate for the 7 dB signal loss incurred in the RG-174U co-ax cable used to connect the modules. The input switch to the PA blocks the mixer's RF signal until full power bias has been applied to the output stage. A DC-DC step-up converter, using an LT1930A (Linear Technologies) switching regulator, provides the 33 V drain voltage to achieve 10 W output power from the NPA1006 amplifier. The VSW2-33-10W+ FET switches cannot make or break their 10 W rated power without damage. This requirement is enforced through a combination of DAQ software and hardware logic in the multiplexer module. The DAQ controls the measurement sequence, setting multiplexer probe select switches before enabling the $\pi/2$ pulse from pulser-mixer.

4.3.3. Pulse Amplifier Delay logic

In the multiplexer module, biasing on the PA is delayed from the start of the $\pi/2$ pulse for the T/R switch to connect to the PA output at low power. This delay logic is shown in figure 5. Here the incoming RF signal from the pulser-mixer is split between the PA's normally open input switch and a discriminator (Linear Technologies LT1711). When the amplitude of the incoming $\pi/2$ pulse exceeds threshold, the discriminator toggles a flip-flop (74HC74) at the reference RF frequency which then continuously triggers a re-triggerable one-shot (74HC123) with delay set longer than twice the RF signal period. While triggered, it sets the TR switch to the output of the idling PA and biases the PA's output stage to achieve full power. The positive transition edge of this 74HC123 triggers a second 74HC123 which, after it times out, clocks a 74HC74 closing the switch at the input of the PA to initiate the 10 W $\pi/2$ pulse to the probe switchyard. After the incoming $\pi/2$ pulse from the pulser-mixer module is completed, the first 74HC123 times out biasing off the PA, connecting the TR switch back to the preamplifier and opening the input switch to the PA. The resulting amplified $\pi/2$ pulse is about a microsecond shorter than that from the pulser-mixer, but the width is still correctly determined by maximizing FID amplitudes.

4.3.4. Preamplifier

Amplification of the microvolt-level FID waveforms returning from probes proceeds in two stages. The first stage consists of a limiter (RLM-33+) followed by an ultra low-noise amplifier (PSA4-5043+), operated at 5 V, and mounted on the same circuit board as the probe switchyard. This first amplifier has a noise figure of 0.73 dB and a gain of 25.4 dB. The limiter protects the low noise amplifier input from fast transients associated with 10 W-excitation pulses. The second stage is an amplifier (Z-KL-1R5) operated at 12 V and located off-board. It has a gain of 41 dB, making the total gain from both stages 66.4 dB. This stage drives the 50 Ω -coax cable connection to the pulser-mixer module.

4.4. Digitizer

The amplified FID signal is digitized with a Struck SIS3316 ADC, where sampling is driven by the 10 MHz reference clock. The digitizer has 16 channels and 16 bit resolution. Frontend software down samples the data to 1 MHz.

4.5. System controller

The interface between the data acquisition computer (DAQ) and the electronic modules is provided by VME standard modules. These include a computer to VME crate controller and waveform digitizers (WFD) from Struck Innovative Systems and an Acromag carrier board with mezzanine modules IP470A and IP-EP201 for digital input and output (DIO) signals.

Three IP470A modules configured as outputs send addresses to multiplexers for probe selection, and one IP-EP201 with field programmable gate array (FPGA) processor Alterra Cyclone II along with code in the DAQ computer executes the rest of the measurement sequence. The IP-EP201 provides a hardware equivalent environment with μ s timing precision to avoid latencies inherent in direct software control of the electronics. FPGA programs are written in VHDL, compiled and synthesized using Alterra's Quartus II development system and compiled code is uploaded to onboard memory via a JTAG port. Within the EP-IP201 environment, individual logic components requiring time synchronization are implemented as processes in the VHDL code, initiated by common clock transitions. These include cascades of logic gates, derived clocks, counters, registers and the state machine that generates the sequence of steps to control the hardware modules previously described.

4.6. Operation modes

Muon injection occurs with a 1.4 s period preceded by a trigger at the start of each injection super cycle when muons are produced in the upstream beam line. This time is sufficient for interrogating all 378 fixed NMR probes. Three operating modes provide different options for the measurement sequence, including running asynchronously or synchronized with muon injection. In mode 1 the system runs asynchronously, taking measurements from all probes based on an internal 1.4 s timer. Muon g-2 production data was generally taken in mode 1. In modes 2 and 3, measurements are synchronized with the start of the injection cycle whenever muons are present. The super cycle timeline has two groups of eight injected muon bunches with 10 ms spacing between bunches. In mode 2, the system makes five measurements per cycle: two coinciding with an injected bunch in each of the two groups and three additional measurements uniformly filling out the cycle. In subsequent cycles, the start of the measurement is shifted to the next bunch in each group. To complete the measurement over all eight bunches, eight super cycles are required. Mode 3 is essentially mode 1, with measurements synchronized to the start of each muon super cycle.

In order to stabilize the field against drift through feedback with the magnet's power supply, continuous periodic field measurements need to be made, whether or not muons are present in the ring. In modes 2 or 3, without accelerator triggers, measurements are triggered by an internal timer, set to the injection cycle period (see Tab. 1 register 34). A second counter, reset by accelerator triggers when present, provides a proxy for phase within the muon injection cycle. A shift register ring counter provides the clock for the measurement timer, which can be varied in frequency by continuously changing which shift register provides the output. When accelerator triggers become available while the system is running in modes 2 or 3, the clock's frequency is *blue-shifted* or *red-shifted* until the measurement timer's phase coincides with the injection cycle phase and measurements proceed triggered externally. Bit 8 in the status register (2e) indicates whether the source of measurement sequence timing is external (1) or internal (0). The firmware is written in VHDL code, which implements the Moore state machine architecture shown on the left side in figure 7. State changes occur on the rising edge of a 1 MHz clock, which determines the timing

precision within the sequence. The right side of the figure represents major steps in the data acquisition code.

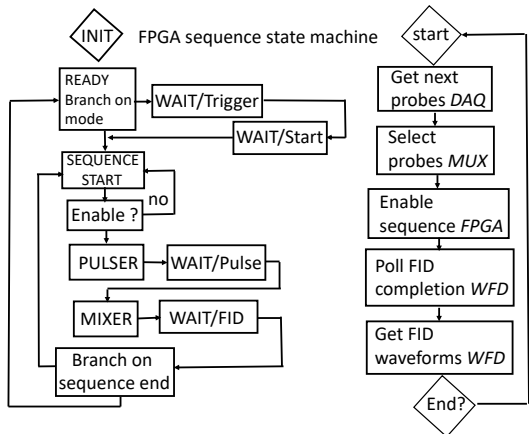


Figure 7: The block diagram on the left shows the Moore State Machine architecture. Rectangular blocks represent individual machine states, and lines with arrows show the program sequence among the states. On the right is the corresponding diagram for code running in the DAQ computer. Together they provide control sequences to execute field measurements.

Referring to figure 7, in a typical measurement scenario, probes are selected in the DAQ using dedicated digital ports and, to allow the measurement sequence to proceed, the enable bit is written to register 20. Depending on the mode, the internal timer or external trigger starts the sequence, and after wait delays enters the pulser state which initiates $\pi/2$ pulses from the pulser electronics and triggers the WFDs to begin digitizing FID waveforms from the mixer electronics in the 20 NIM pulser-mixer modules. The mixer state then starts a timed pause of the sequence which exceeds the time required for the DAQ cycle to complete. When the WFDs signal completion, waveforms are uploaded and the DAQ cycle restarts, re-enabling the state machine. When the pause timer completes, the sequence restarts, providing a periodic time series of probe measurements at precise intervals.

In addition to state machine and timer processes, the VHDL implementation includes VME accessible registers to set timer durations, enable the sequence and read timestamps. These are listed by their address offsets and whether they have read (R) or write (W) access in table 1. The first two registers configure board pins as outputs for triggering pulser modules and WFDs, or inputs for external clock event signals. After multiplexers are

Table 1: VME accessible registers

Offset (hex)	Register Description
02 RW	configure DIO pins 1 - 16
04 RW	configure DIO pins 17 - 32
20 W	multiplexer ready
22 RW	start delay time
24 RW	bunch delay time
26 RW	FID delay time
28 RW	operating mode
2a R	FID timestamp low
2c R	FID timestamp high
2e RW	sequence status
30 RW	sequence parameters
32 R	T_0 timestamp (external source)
34 RW	measurement period

addressed, writing 1 to the register 20 enables starting the FID sequence. Registers 22 to 26 configure the internal timers used in sequencing between machine states. Times are specified in units of $10 \mu\text{s}$. Register 28 sets the operating mode (modes 1, 2, 3). Registers 2a and 2c are the low and high words of the 32 bit measurement time stamp written to the data file. Times are in units of microseconds elapsed since the previous external synchronization signal. Register 2e gives the status of read sequences (current sequence ID). Register 30 sets operating mode specific parameters. Register 32 gives the internal clock time of a second external event signal input to the board. Register 34 sets the period of the internal measurement cycle timer.

5. Performance of the fixed-probe system

In this section we introduce performance metrics for the fixed probe magnetometer. These include

- in situ measurement resolutions of individual NMR probes.
- a measure of probe performance independent of the local field environment.
- system component performance over the lifetime of the experiment.
- an example demonstrating the utility of good timing precision in the system controller.

Magnetometer field measurements are given by proton precession frequencies obtained from FIDs,

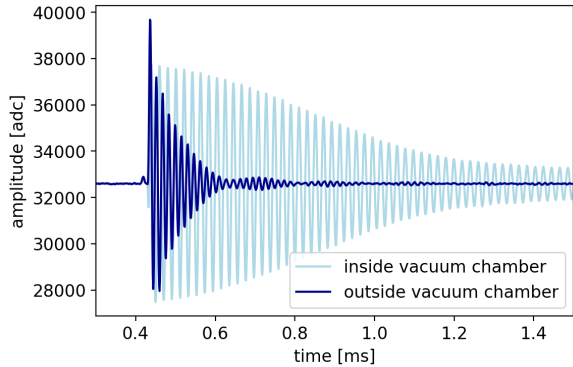


Figure 8: Two free induction decay waveforms (FID), one from the fixed probe magnetic environment of the inflector vacuum chamber wall and the other further from pole pieces in the muon storage vacuum. The probes are located at the same azimuthal position but in regions with very different field gradients. Their FID signals are characteristic of the two very different magnetic environments, with the rest of the probe waveforms lying somewhere in between.

using the procedures outlined in reference [5]. Field gradients along the sensitive volume of the probe result in variations in the precession frequency of the sample within the probe’s volume. The phases are initially synchronized at the $\pi/2$ pulse but decohere with time constant T^* , which shortens the length of the FID. Frequency resolution scales with the inverse of the measurement time available for analysis. To smooth out field variations along the axis of the probes, shims were added to pole faces in the vicinity of the NMR probes. While this effort was largely successful, these shims were incorrectly positioned around the inflector vacuum chamber, where muons are injected, and significant field gradients remained. Figure 8 shows FID waveforms from two fixed probes in that chamber. One is embedded in the vacuum chamber wall and the other is inside the vacuum chamber away from the pole faces. These two probes are at the same azimuthal position but in different field gradients, represent the shortest and longest FID waveforms of the fixed probes in the storage ring. A comparison of the FID and the noise in power spectral density is shown in figure 9.

Frequency resolutions of all 378 probes are shown in figure 10. These are standard deviations of 10 consecutive frequency readings. The vertical axis is the multiplexer (MUX) connected to the probe and the horizontal axis is the read cycle of all MUXs. The inflector region, known to have large field gradients has probes that connect to multi-

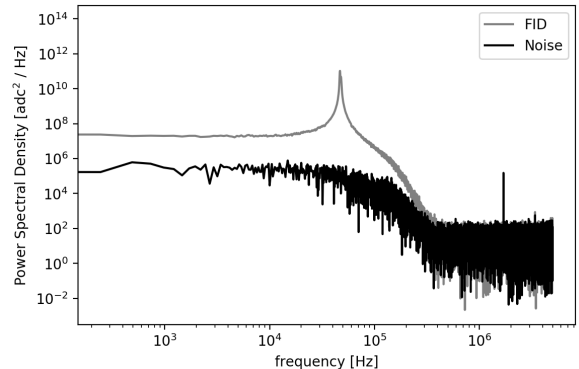


Figure 9: Power spectral density of an FID and pure noise. The noise data are taken while the magnet was turned off but with the same trigger and readout sequence. The higher plateau at low frequencies is caused by the envelope of the FID, while the peak is caused by the spin precession frequency. The effect of high frequency filtering can be seen in both the noise and FID spectra.

plexers MUX 1 and MUX 20. The poor resolution outliers are clearly visible at the top and bottom of the figure. Multiplexers’ locations are roughly symmetric in storage ring azimuth. The darker horizontal band in the center of the figure corresponds to the opposite side of the ring from the inflector region and indicates larger field gradients there as well. Probe resolutions in the fixed probe magnetic field environment range from 3.1 ppb to 1.3 ppm with a median resolution of 11 ppb. All 378 NMR probes were used to determine the azimuthally averaged magnetic field for the muon g-2 experiment.

Frequency resolution, while the important metric, depends on the local magnetic field homogeneity achieved by the shimming process. A measure of intrinsic performance less dependent on the local environment is the probe’s signal-to-noise ratio (SNR), which is calculated from the peak of the signal power spectral density and noise taken when the field was off. Figure 9 shows Fourier power spectra from a typical probe. Individual probe SNRs are given in figure 11 by multiplexer and readout cycle number. Data was taken during the last run of the experiment and probe SNRs continue to range between 50 dB and 60 dB with some outliers from probes in large field gradient regions. The large number of probes provided good spacial resolution over the storage ring azimuth.

Contributing to the excellent performance and longevity, electrical connections within the series resonant circuit that surrounds the probe’s proton

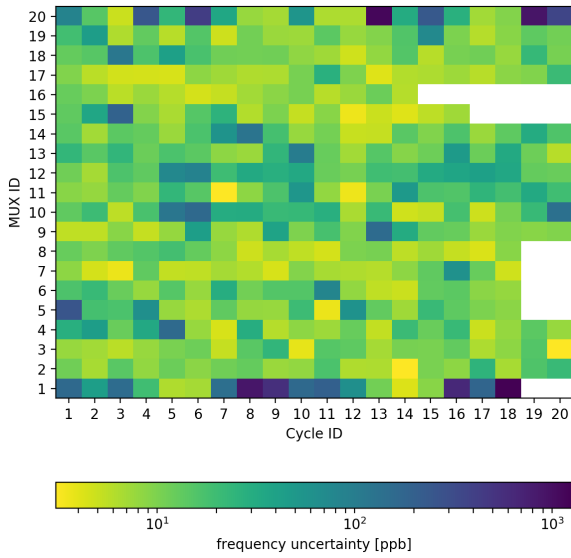


Figure 10: Single shot frequency determination uncertainty for each probe indexed by MUX and readout cycle number (individual probe in the MUX). Uncertainties are calculated from standard deviations of consecutive FID waveforms. Due to different field gradient strengths in the magnetic environment of each probe, frequency uncertainties vary from 3.1 ppb to 1.3 ppm. The median uncertainty is 11 ppb.

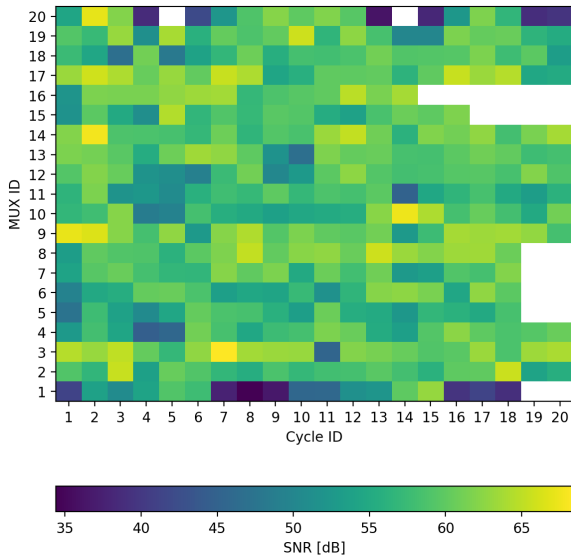


Figure 11: Signal to noise ratio (SNR) from maximal peak of power spectral density (PSD) spectra of each fixed probe indexed by MUX and readout cycle number (individual probe in the MUX). The SNR was calculated at the PSD peak position.

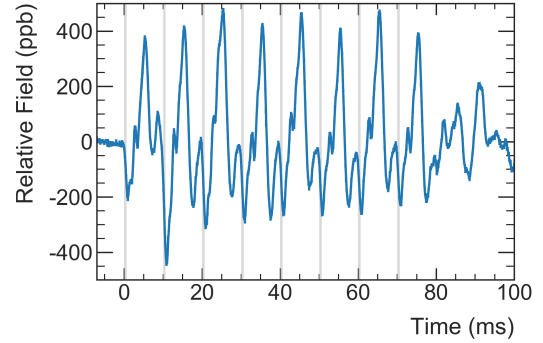


Figure 12: Composite plot of the transient magnetic field measured at the center of electrostatic quadrupole Q3L. The persistent field transient is sampled by continuously increasing measurement start time delays at each subsequent muon injection cycle. The plot shows the time series of these samples. Vertical lines are the times of muon bunches, when electrostatic quadrupoles are pulsed on. Figure from [14].

sample were either crimped or soldered, resulting in a low overall resistance and quality factor $Q = 60$. The comparable Q of those BNL E821 probes still operational in 2013 was 30. The resonant amplification factor of the circuit scales with Q on resonance and contributes to the improved signal-to-noise ratio of E989 probes. All fixed probes and probes in the measurement trolley continue to provide quality field measurements after six years.

While this section emphasizes individual probes, the true performance measure of the magnetometer was demonstrated by magnetic field measurements in the E989 experiment; see for example references [14], [15]. In general, the fixed probe system surpassed its design requirements. In the latest published result of measurement campaigns 2 and 3, the overall magnetic field uncertainty was 52 ppb [16] which is well below the technical design report goal of 70 ppb [4] and the uncertainty attributed to magnetic field monitoring over time of 17 ppb surpassed the design requirement of 20 ppb as well.

The superferric storage ring magnet operates in non-persistence mode at a current around 5170 Amps. Temperature variation in the experimental hall and pressure fluctuations in the cryogenic system result in magnetic field fluctuations. Based on fixed probe magnetometer measurements, a current feedback system in the magnet's power supply provides temporal stabilization of the magnetic field at the ppm scale. Its excellent performance is further detailed in [17].

5.1. Electrostatic Quadrupole Transients

When measuring asynchronously (mode 1), fixed probes located in vacuum chambers containing electrostatic quadrupoles (ESQ) showed larger rms variations than probes in vacuum chambers without them. Muons are constrained vertically in the storage ring by these electrostatic quadrupoles, which are pulsed at 100 Hertz, corresponding to the muon beam injection. Synchronizing measurements with these bunches showed previously unknown fast magnetic field transients. We determined Lorentz forces induce vibrations in quadrupole electrodes, generating the fast magnetic transients by eddy currents.

The average storage ring magnetic field is measured every 1.4s. While muons occupy the storage volume less than 1% of that time they do experience these transient fields. The 1 μ s precision of the sequencer programmed in the IP-EP201 FPGA allowed precision time scanning of field measurements across the duration of muon bunches, where the measurement start time delay is increased at each injection cycle. High frequency magnetic field oscillations are strongly attenuated by the aluminum vacuum chamber walls and require a custom probe assembly inside the vacuum region to measure them.

When muons were not being stored in the ring, an NMR probe, sealed against vacuum, was placed at the center of the electrostatic quadrupole (near zero electric fields) and measurements were taken while the quadrupole were pulsing. The time series of these scans shown in figure 12 is the aliased persistent magnetic transient waveform seen by muons measured with NMR precision.

6. Summary

The E989 muon g-2 experiment at Fermi National Accelerator Laboratory aims for a twofold reduction of systematic uncertainties in storage ring field measurements compared with BNL E821 requiring ppb level accuracy. The technique of pulsed proton NMR is capable of part per billion uncertainties and, following BNL, it was used here as well. The fixed probe magnetometer continually tracks the magnetic field whether or not muons are in the storage ring. NMR probes were completely redesigned with robust construction techniques and RF electronic modules were developed using modern modular electronics. All 378 NMR probes em-

bedded in the ring vacuum chamber walls were operational providing a uniform sampling of the magnetic field in azimuth. The initial systematic goals of the experiment were more than met by this magnetometer.

Acknowledgments

We thank Fermilab management for providing funding for magnetometer construction, the UW Physics Department machine shop for precision machining of parts for more than 450 NMR probes and the CENPA staff for help in navigating the procurement process and providing resources for establishing the 1.45 T field for testing the system. We thank Dr. Simon Corrodi for sharing his analysis results in figure 12. This work was supported by the DOE Offices of Nuclear Physics (DE-FG02-97ER41020). Prof. Dr Martin Fertl and Dr. René Reimann receive support from the Cluster of Excellence “Precision Physics, Fundamental Interactions, and Structure of Matter” (PRISMA+ EXC 2118/1) funded by the German Research Foundation (DFG) within the German Excellence Strategy (Project ID 39083149).

7. Appendices

7.1. Probe assembly process

More than 450 pNMR probes were assembled efficiently and reproducibly. We developed a standard assembly procedure based on an *assembly kit* that contained all parts required to assemble an individual probe from start to finish. Such an assembly kit is shown in figure 13. In addition, we developed several mechanical tools to ensure precise assembly of the mechanically delicate parts. In the next subsections we give examples of procedures used in the preparation of individual parts and sub-assemblies and present some of the special tools used in the assembly process.

7.1.1. Cleaning procedure for the PTFE parts

Machining fluid residues from all parts made from PTFE were removed with a three stage cleaning procedure:

- 20 min of ultrasonic cleaning in pure acetone heated to 60 °C.
- 5 min of ultrasonic cleaning in pure 2-propanol heated to 60 °C.



Figure 13: A typical assembly kit for a single NMR probe containing all required construction pieces. For quality control purposes, the individual assembler of the probe are indicated on the bag and each probe was assigned a unique identification number.

- 5 min of ultrasonic cleaning in deionized water followed by overnight drying at room temperature.

Any handling of parts was performed with gloved hands.

7.1.2. Cleaning procedure for the aluminum parts

Machining fluid residues from aluminum parts were removed with a similar three stage cleaning procedure:

- 20 min of ultrasonic cleaning in pure 2-propanol heated to 60 °C.
- Rinsing with deionized water.
- 5 min of ultrasonic cleaning in deionized water. Removal of all remaining water with lint-free laboratory grade wipes, followed by overnight drying at room temperature.

Gloves were also required for handling these parts.

7.1.3. Filling the sample holder with petroleum jelly

The petroleum jelly and *sample holder* are pre-heated and maintained at about 80 °C during the filling process in order to have enough handling time. The setup used to fill seven *sample holder* cavities at a time is shown in figure 14.

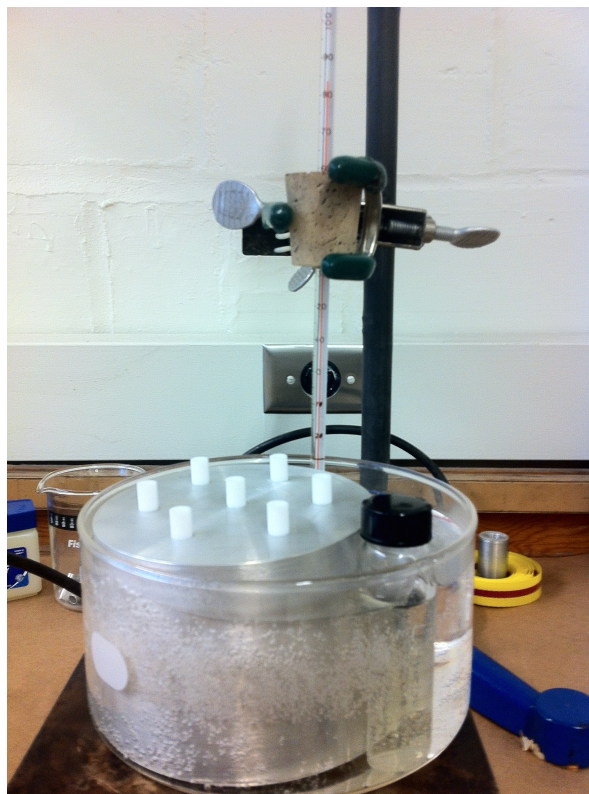


Figure 14: This fill station was used to melt the petroleum jelly in a water bath on top of a heater plate which was also used to pre-heat the *sample holder*. A glass jar with molten petroleum jelly can be seen to the right of the aluminum block.

The following procedure helped ensure that no air bubbles were introduced in the sample cavity

1. **Warming the *sample holder*:** Place the *sample holder* holding block into the water bath and warm it up to 90 °C.
2. **Melting the petroleum jelly:** Melt the petroleum jelly in a glass jar by putting it into the hot water bath next to the Al block. Warm the petroleum jelly until its viscosity is low enough that it can be sucked into the syringe through a blunt stainless steel needle (gauge 16).

3. **Preheating the glass syringe:** Preheat the glass syringe in a heated jacket regulated to 85 °C to prevent the petroleum jelly in the glass syringe from becoming solid. Install the stainless steel needle with Luer lock onto the glass syringe.
4. **Preheating the *sample holder* pieces:** Load seven *sample holder* pieces into the holes of the holes of the aluminum block and wait some minutes until all sample holders warmed up to the temperature of the Al block.
5. **Transfer of petroleum jelly:** Take the preheated glass syringe and bring the needle into the glass jar with the molten petroleum jelly. Allow the needle to heat up for some seconds before you try to fill the syringe. Draw in about 5 mL of the molten petroleum jelly. Stick the stainless steel needle into the sample volume of the *sample holder* until it reaches the bottom of the cavity. Slowly inject petroleum jelly into the sample space while retracting the needle (This is important as just pulling the needle out causes bubbles to form). DO NOT overfill the sample space. Fill it up to the middle of the thread for the *inner conductor*.
6. **Remove any air bubbles:** If during inspection of the sample space air bubbles are detected they can be removed by lowering the needle again to the bottom of the cavity and by injecting more petroleum jelly. Alternatively one can suck the air bubble back into the needle/syringe. The first way is highly recommended.
7. **Cool down:** Remove the aluminum block from the water bath and let the whole block cool down to room temperature.

Two filled sample holders are shown in figure 15.

7.1.4. Winding the serial inductor coil

The wire of the inductor coil is first pressed into its dedicated groove in the *sample holder* (this protects the wire varnish from being scraped off by the aluminum sleeve installed in a later step) and the first three turns were wound manually. Coil windings are guided by external M4.5x0.5 threads in the bottom of the coil region. This allowed maintaining a constant tension on the wire during the winding process. After this, an aluminum sleeve (see figure 15) was attached to protect the *sample holder* from ferromagnetic impurities of the machine chuck



Figure 15: Two sample holders shown with their sample cavities filled with petroleum jelly (slight yellow tint). Aluminum sleeves that protect the *sample holder* during winding of the serial inductor coil are also depicted here.

on the coil winding machine. The coil winding machine shown in figure 16 was used to wind the remaining 29 coil turns into the threads. To avoid bending the *sample holder* during the winding process a dead center made from plastic was used on the far end of the *sample holder* (also shown in the figure). After all 32 turns have been wound the free wire end was secured in the second half of the dedicated wire groove. All part handling was performed with gloved hands to protect the clean parts. A set of two finished series inductor coils is shown in figure 17.

7.1.5. Soldering a wire loop on the inner conductor

The serial inductor coil is connected to the *inner conductor* in a two-step procedure. First a wire loop is soldered to the aluminum inner conductor using a flux-less, ultrasonic soldering technique. This reduces the risk of long-term corrosion-induced contact failure. The power of the ultrasonic soldering iron is insufficient to heat the *in-*

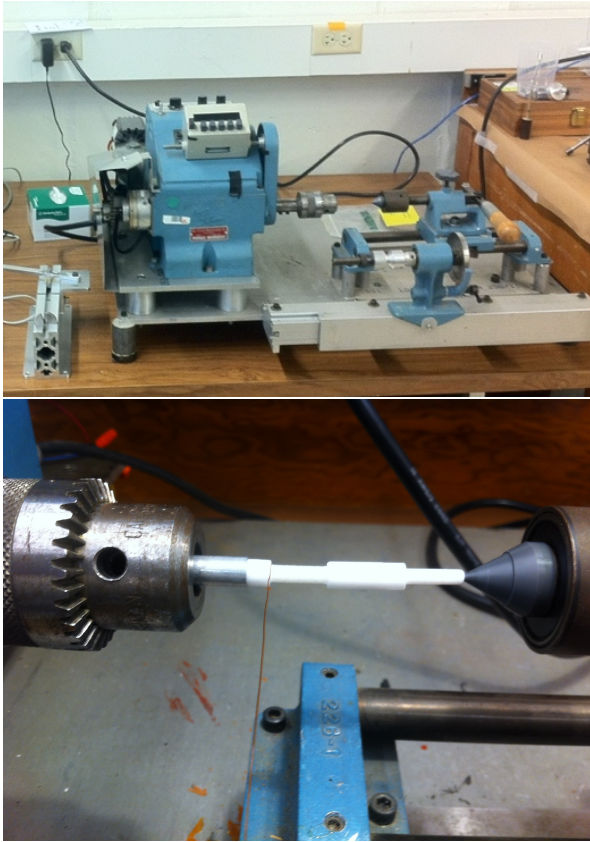


Figure 16: The series inductor coils were wound with a refurbished slowly rotating coil winding machine. The gray box on top of the blue motor box is a turn counter. Only non-ferromagnetic material is in physical contact with the PTFE sample holder.

ner conductor pieces to the solder melting point so they were preheated by screwing them into a copper block sitting on a hot plate, see figure 18. In the second step, the series inductor coil is soldered to the wire loop.

The ultrasonic soldering procedure:

1. **Forming of the loop:** A short (1 inch) piece of bare AWG 26 magnet wire is pulled through the 1 mm diameter hole in the *inner conductor* such that a small loop is remaining on one side that prevents the wire from falling through the hole.
2. **Securing the wire:** The wire is secured in the hole by bending the two wire ends in opposite directions around the *inner conductor*, as shown in figure 19.
3. **Heating of the *inner conductor* to soldering temperature:** The prepared inner con-

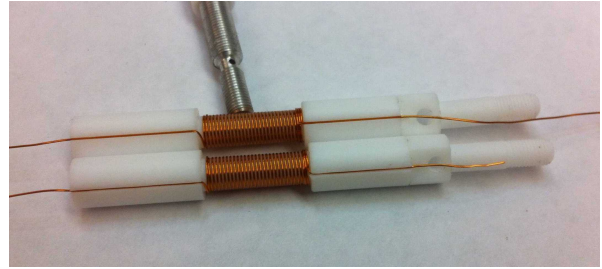


Figure 17: A set of two finished series inductor coils wound on their PTFE sample holder.

ductor pieces are screwed into threaded holes (M4x0.5) in a copper block sitting on a hot plate heated to 200 °C (as measured by a thermocouple attached to the copper block)

4. **Ultrasonic soldering process:** The temperature of the ultrasonic soldering iron is set to 200 °C and left to heat up. The ultrasonic soldering iron uses special solder (CERASOLZER ALU-200, 1.6 mm diameter) that melts at this temperature. The tip of the soldering iron is placed at the surface of the *inner conductor* piece where the two wire ends bend around the surface. Only a small quantity of solder is needed at the joint. Apply ultrasonic power by pressing down on the step-on switch below the table. The solder will start to wet the surfaces after applying the ultrasonic power.

7.1.6. Assembly database

We maintained a database to record the assembly history and quality checks for each probe. It is accessed by the probe's unique identification number. It includes the person responsible for assembling the probe and the date assembly was completed. After assembly the series LC circuit in each probe was tuned to 61.74 MHz by observing the reflection plot when connected to a vector network analyzer. Tuning occurs by varying the probe capacitance with a specially designed tool through the probe's end cap. The impedance is given by the attenuation of the reflected signal at resonance. Tuning this parameter requires opening the probe and deforming a few turn coil parallel to the series resonant circuit. The database includes all plots and analyzed data for the probes. It is a reference for the initial probe qualities once the probes are installed at Fermilab.

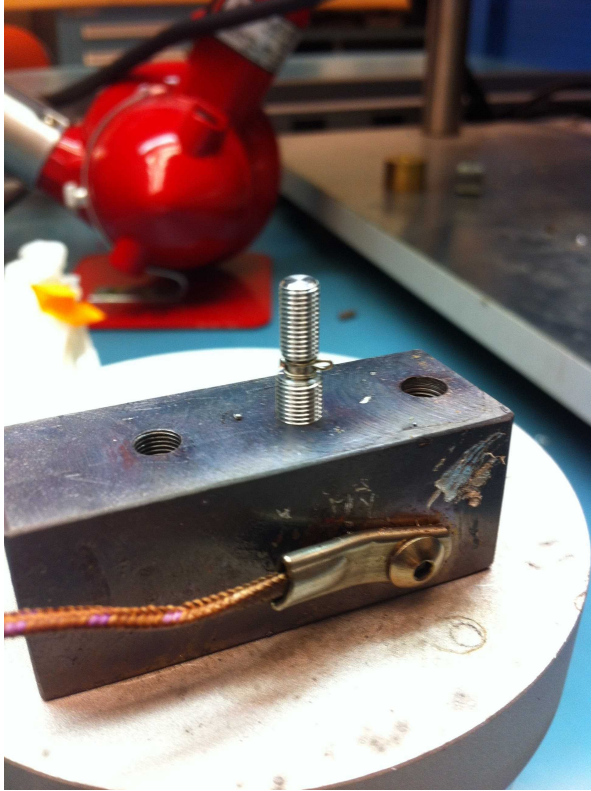


Figure 18: One inner conductor piece screwed into a copper block with threaded holes sitting on a hot plate to facilitate the ultrasonic soldering process.



Figure 19: Soldering the connection loop into the *inner conductor* is performed with an ultrasonic soldering iron.

References

- [1] G. W. Bennett, B. Bousquet, H. N. Brown, G. Bunce, R. M. Carey, P. Cushman, G. T. Danby, P. T. Debevec, M. Deile, H. Deng, W. Deninger, S. K. Dhawan, V. P. Druzhinin, L. Duong, E. Efsthadiadis, F. J. M. Farley, G. V. Fedotovitch, S. Giron, F. E. Gray, D. Grigoriev, M. Grosse-Perdekamp, A. Grossmann, M. F. Hare, D. W. Hertzog, X. Huang, V. W. Hughes, M. Iwasaki, K. Jungmann, D. Kawall, M. Kawamura, B. I. Khazin, J. Kindem, F. Krienen, I. Kronkvist, A. Lam, R. Larsen, Y. Y. Lee, I. Logashenko, R. McNabb, W. Meng, J. Mi, J. P. Miller, Y. Mizumachi, W. M. Morse, D. Nikas, C. J. G. Onderwater, Y. Orlov, C. S. Özben, J. M. Paley, Q. Peng, C. C. Polly, J. Pretz, R. Prigl, G. zu Putlitz, T. Qian, S. I. Redin, O. Rind, B. L. Roberts, N. Ryskulov, S. Sedych, Y. K. Semertzidis, P. Shagin, Y. M. Shatunov, E. P. Sichtermann, E. Solodov, M. Sossong, A. Steinmetz, L. R. Sulak, C. Timmermans, A. Trofimov, D. Urner, P. von Walter, D. Warburton, D. Winn, A. Yamamoto, D. Zimmerman, Final report of the e821 muon anomalous magnetic moment measurement at bnl, *Phys. Rev. D* 73 (2006) 072003. doi:10.1103/PhysRevD.73.072003. URL <https://link.aps.org/doi/10.1103/PhysRevD.73.072003>
- [2] R. Prigl, U. Haeberlen, K. Jungmann, G. zu Putlitz, P. von Walter, A high precision magnetometer based on pulsed nmr, *Nuclear Instruments and Methods in Physics Research Section A: Accelerators, Spectrometers, Detectors and Associated Equipment* 374 (1) (1996) 118 – 126. doi:https://doi.org/10.1016/0168-9002(96)37493-7. URL <http://www.sciencedirect.com/science/article/pii/0168900296374937>
- [3] W. D. Phillips, W. E. Cooke, D. Kleppner, Magnetic moment of the proton in h₂o in bohr magnetons, *Metrologia* 13 (4) (1977) 179. doi:10.1088/0026-1394/13/4/005. URL <https://dx.doi.org/10.1088/0026-1394/13/4/005>
- [4] Muon (g-2) technical design report (2018). arXiv:1501.06858.
- [5] R. Hong, S. Corrodi, S. Charity, S. Baeßler, J. Bono, T. Chupp, M. Fertl, D. Flay, A. García, J. George, K. L. Giovanetti, T. Gorringer, J. Grange, K. W. Hong, D. Kawall, B. Kiburg, B. Li, L. Li, R. Ososky, D. Počanić, S. Ramachandran, M. Smith, H. E. Swanson, A. Tewsley-Booth, P. Winter, T. Yang, K. Zheng, Systematic and statistical uncertainties of the hilbert-transform based high-precision fid frequency extraction method, *Journal of Magnetic Resonance* 329 (2021) 107020. doi:https://doi.org/10.1016/j.jmr.2021.107020. URL <https://www.sciencedirect.com/science/article/pii/S1090780721001099>
- [6] S. Corrodi, P. D. Lurgio, D. Flay, J. Grange, R. Hong, D. Kawall, M. Oberling, S. Ramachandran, P. Winter, Design and performance of an in-vacuum, magnetic field mapping system for the muon g-2 experiment, *Journal of Instrumentation* 15 (11) (2020) P11008–P11008. doi:10.1088/1748-0221/15/11/p11008. URL <https://doi.org/10.1088/1748-0221/15/11/p11008>
- [7] D. Flay, D. Kawall, T. Chupp, S. Corrodi, M. Farooq,

- M. Fertl, J. George, J. Grange, R. Hong, R. Osofsky, S. Ramachandran, E. Swanson, P. Winter, High-accuracy absolute magnetometry with application to the fermilab muon $g-2$ experiment, *Journal of Instrumentation* 16 (12) (2021) P12041. doi:10.1088/1748-0221/16/12/P12041.
URL <https://dx.doi.org/10.1088/1748-0221/16/12/P12041>
- [8] M. Farooq, T. Chupp, J. Grange, A. Tewsley-Booth, D. Flay, D. Kawall, N. Sachdeva, P. Winter, Absolute Magnetometry with ^3He , *Physical Review Letters* 124 (22) (2020) 223001. doi:10.1103/PhysRevLett.124.223001.
- [9] E. Tiesinga, P. J. Mohr, D. B. Newell, B. N. Taylor, CODATA recommended values of the fundamental physical constants: 2018, *Rev. Mod. Phys.* 93 (2021) 025010. doi:10.1103/RevModPhys.93.025010.
URL <https://link.aps.org/doi/10.1103/RevModPhys.93.025010>
- [10] J. Keeler, *Understanding NMR Spectroscopy*, Wiley, 2002.
- [11] F. Bloch, Nuclear induction, *Phys. Rev.* 70 (1946) 460–474. doi:10.1103/PhysRev.70.460.
URL <https://link.aps.org/doi/10.1103/PhysRev.70.460>
- [12] <http://www.sonicsolder.com/>.
- [13] Mini-circuits product catalog, https://www.minicircuits.com/pdfs/Complete%20Catalog_2021_Digital.pdf (2021).
- [14] T. Albahri, A. Anastasi, K. Badgley, S. Baeßler, I. Bailey, V. A. Baranov, E. Barlas-Yucel, T. Barrett, F. Bedeschi, M. Berz, M. Bhattacharya, H. P. Binney, P. Bloom, J. Bono, E. Bottalico, T. Bowcock, G. Cantatore, R. M. Carey, B. C. K. Casey, D. Cauz, R. Chakraborty, S. P. Chang, A. Chapelain, S. Charity, R. Chislett, J. Choi, Z. Chu, T. E. Chupp, A. Conway, S. Corrodi, L. Cotrozzi, J. D. Crnkovic, S. Dabagov, P. T. Debevec, S. Di Falco, P. Di Meo, G. Di Sciascio, R. Di Stefano, A. Driutti, V. N. Duginov, M. Eads, J. Esquivel, M. Farooq, R. Fatemi, C. Ferrari, M. Fertl, A. T. Fienberg, A. Fioretti, D. Flay, N. S. Froemming, C. Gabbanini, M. D. Galati, S. Ganguly, A. Garcia, J. George, L. K. Gibbons, A. Gioiosa, K. L. Giovanetti, P. Girotti, W. Gohn, T. Gorringer, J. Grange, S. Grant, F. Gray, S. Haciomeroglu, T. Halewood-Leagas, D. Hampai, F. Han, J. Hempstead, A. T. Herrod, D. W. Hertzog, G. Hesketh, A. Hibbert, Z. Hodge, J. L. Holzbauer, K. W. Hong, R. Hong, M. Iacovacci, M. Incagli, P. Kammel, M. Kargiantoulakis, M. Karuza, J. Kaspar, D. Kawall, L. Kelton, A. Keshavarzi, D. Kessler, K. S. Khaw, Z. Khechadorian, N. V. Khomutov, B. Kiburg, O. Kim, Y. I. Kim, B. King, N. Kinnaird, E. Kraegeloh, N. A. Kuchinskiy, K. R. Labe, J. LaBounty, M. Lancaster, M. J. Lee, S. Lee, B. Li, D. Li, L. Li, I. Logashenko, A. Lorente Campos, A. Lucà, G. Lukicov, A. Lusiani, A. L. Lyon, B. MacCoy, R. Madrak, K. Makino, F. Marignetti, S. Mastroianni, J. P. Miller, S. Miozzi, W. M. Morse, J. Mott, A. Nath, H. Nguyen, R. Osofsky, S. Park, G. Pauletta, G. M. Piacentino, R. N. Pilato, K. T. Pitts, B. Plaster, D. Počanić, N. Pohlman, C. C. Polly, J. Price, B. Quinn, N. Raha, S. Ramachandran, E. Ramberg, J. L. Ritchie, B. L. Roberts, D. L. Rubin, L. Santi, C. Schlesier, A. Schreckenberger, Y. K. Semertzidis, D. Shemyakin, M. W. Smith, M. Sorbara, D. Stöckinger, J. Stapleton, C. Stoughton, D. Stratakis, T. Stuttard, H. E. Swanson, G. Sweetmore, D. A. Sweigart, M. J. Syphers, D. A. Tarazona, T. Teubner, A. E. Tewsley-Booth, K. Thomson, V. Tishchenko, N. H. Tran, W. Turner, E. Valetov, D. Vasilkova, G. Venanzoni, T. Walton, A. Weisskopf, L. Welty-Rieger, P. Winter, A. Wolski, W. Wu, Magnetic-field measurement and analysis for the muon $g - 2$ experiment at fermilab, *Phys. Rev. A* 103 (2021) 042208. doi:10.1103/PhysRevA.103.042208.
URL <https://link.aps.org/doi/10.1103/PhysRevA.103.042208>
- [15] T. Albahri, A. Anastasi, A. Anisenkov, K. Badgley, S. Baeßler, I. Bailey, V. A. Baranov, E. Barlas-Yucel, T. Barrett, A. Basti, F. Bedeschi, M. Berz, M. Bhattacharya, H. P. Binney, P. Bloom, J. Bono, E. Bottalico, T. Bowcock, G. Cantatore, R. M. Carey, B. C. K. Casey, D. Cauz, R. Chakraborty, S. P. Chang, A. Chapelain, S. Charity, R. Chislett, J. Choi, Z. Chu, T. E. Chupp, S. Corrodi, L. Cotrozzi, J. D. Crnkovic, S. Dabagov, P. T. Debevec, S. Di Falco, P. Di Meo, G. Di Sciascio, R. Di Stefano, A. Driutti, V. N. Duginov, M. Eads, J. Esquivel, M. Farooq, R. Fatemi, C. Ferrari, M. Fertl, A. T. Fienberg, A. Fioretti, D. Flay, E. Frlež, N. S. Froemming, J. Fry, C. Gabbanini, M. D. Galati, S. Ganguly, A. Garcia, J. George, L. K. Gibbons, A. Gioiosa, K. L. Giovanetti, P. Girotti, W. Gohn, T. Gorringer, J. Grange, S. Grant, F. Gray, S. Haciomeroglu, T. Halewood-Leagas, D. Hampai, F. Han, J. Hempstead, A. T. Herrod, D. W. Hertzog, G. Hesketh, A. Hibbert, Z. Hodge, J. L. Holzbauer, K. W. Hong, R. Hong, M. Iacovacci, M. Incagli, P. Kammel, M. Kargiantoulakis, M. Karuza, J. Kaspar, D. Kawall, L. Kelton, A. Keshavarzi, D. Kessler, K. S. Khaw, Z. Khechadorian, N. V. Khomutov, B. Kiburg, M. Kiburg, O. Kim, Y. I. Kim, B. King, N. Kinnaird, E. Kraegeloh, A. Kuchibhotla, N. A. Kuchinskiy, K. R. Labe, J. LaBounty, M. Lancaster, M. J. Lee, S. Lee, S. Leo, B. Li, D. Li, L. Li, I. Logashenko, A. Lorente Campos, A. Lucà, G. Lukicov, A. Lusiani, A. L. Lyon, B. MacCoy, R. Madrak, K. Makino, F. Marignetti, S. Mastroianni, J. P. Miller, S. Miozzi, W. M. Morse, J. Mott, A. Nath, H. Nguyen, R. Osofsky, S. Park, G. Pauletta, G. M. Piacentino, R. N. Pilato, K. T. Pitts, B. Plaster, D. Počanić, N. Pohlman, C. C. Polly, J. Price, B. Quinn, N. Raha, S. Ramachandran, E. Ramberg, J. L. Ritchie, B. L. Roberts, D. L. Rubin, L. Santi, C. Schlesier, A. Schreckenberger, Y. K. Semertzidis, D. Shemyakin, M. W. Smith, M. Sorbara, D. P. Aguillard, T. Albahri, D. Allspach, A. Anisenkov, K. Badgley, S. Baeßler, I. Bailey, L. Bailey, V. A. Baranov, E. Barlas-Yucel, T. Barrett, E. Barzi, F. Bedeschi, M. Berz, M. Bhattacharya, H. P. Binney,

P. Bloom, J. Bono, E. Bottalico, T. Bowcock, S. Braun, M. Bressler, G. Cantatore, R. M. Carey, B. C. K. Casey, D. Cauz, R. Chakraborty, A. Chapelain, S. Chappa, S. Charity, C. Chen, M. Cheng, R. Chislett, Z. Chu, T. E. Chupp, C. Claessens, M. E. Convery, S. Corrodi, L. Cotrozzi, J. D. Crnkovic, S. Dabagov, P. T. Debevec, S. Di Falco, G. Di Sciascio, S. Donati, B. Drendel, A. Driutti, V. N. Duginov, M. Eads, A. Edmonds, J. Esquivel, M. Farooq, R. Fatemi, C. Ferrari, M. Fertl, A. T. Fienberg, A. Fioretti, D. Flay, S. B. Foster, H. Friedsam, N. S. Froemming, C. Gabbanini, I. Gaines, M. D. Galati, S. Ganguly, A. Garcia, J. George, L. K. Gibbons, A. Gioiosa, K. L. Giovanetti, P. Girotti, W. Gohn, L. Goodenough, T. Goringe, J. Grange, S. Grant, F. Gray, S. Haciomeroglu, T. Halewood-Leagas, D. Hampai, F. Han, J. Hempstead, D. W. Hertzog, G. Hesketh, E. Hess, A. Hibbert, Z. Hodge, K. W. Hong, R. Hong, T. Hu, Y. Hu, M. Iacovacci, M. Incagli, P. Kammel, M. Kargiantoulakis, M. Karuza, J. Kaspar, D. Kawall, L. Kelton, A. Keshavarzi, D. S. Kessler, K. S. Khaw, Z. Khechadorian, N. V. Khomutov, B. Kiburg, M. Kiburg, O. Kim, N. Kinnaird, E. Kraegeloh, V. A. Krylov, N. A. Kuchinskiy, K. R. Labe, J. LaBounty, M. Lancaster, S. Lee, B. Li, D. Li, L. Li, I. Logashenko, A. L. Campos, Z. Lu, A. Lucà, G. Lukicov, A. Lusiani, A. L. Lyon, B. MacCoy, R. Madrak, K. Makino, S. Mastroianni, J. P. Miller, S. Miozzi, B. Mitra, J. P. Morgan, W. M. Morse, J. Mott, A. Nath, J. K. Ng, H. Nguyen, Y. Okuzian, Z. Omarov, R. Osofsky, S. Park, G. Pauletta, G. M. Piacentino, R. N. Pilato, K. T. Pitts, B. Plaster, D. Počanić, N. Pohlman, C. C. Polly, J. Price, B. Quinn, M. U. H. Qureshi, S. Ramachandran, E. Ramberg, R. Reimann, B. L. Roberts, D. L. Rubin, M. Sakurai, L. Santi, C. Schlesier, A. Schreckenberger, Y. K. Semertzidis, D. Shemyakin, M. Sorbara, J. Stapleton, D. Still, D. Stöckinger, C. Stoughton, D. Stratakis, H. E. Swanson, G. Sweetmore, D. A. Sweigart, M. J. Syphers, D. A. Tarazona, T. Teubner, A. E. Tewsley-Booth, V. Tishchenko, N. H. Tran, W. Turner, E. Valetov, D. Vasilkova, G. Venanzoni, V. P. Volnykh, T. Walton, A. Weisskopf, L. Welty-Rieger, P. Winter, Y. Wu, B. Yu, M. Yucel, Y. Zeng, C. Zhang, Detailed Report on the Measurement of the Positive Muon Anomalous Magnetic Moment to 0.20 ppm (Feb. 2024). [arXiv:2402.15410](https://arxiv.org/abs/2402.15410), [doi:10.48550/arXiv.2402.15410](https://doi.org/10.48550/arXiv.2402.15410).

- [17] Muon g-2 Collaboration, P. D. Aguillard, et al., Operations of the Muon g-2 experiment at Fermilab (E989) *in preperation*.